A Decadal-Scale Teleconnection between the North Atlantic Oscillation and Subtropical Eastern Australian Rainfall

CHENG SUN

College of Global Change and Earth System Science, Beijing Normal University, and State Key Laboratory of Numerical Modeling for Atmospheric Sciences and Geophysical Fluid Dynamics (LASG), Institute of Atmospheric Physics, Chinese Academy of Sciences, Beijing, China

JIANPING LI

College of Global Change and Earth System Science, Beijing Normal University, and Joint Center for Global Change Studies, Beijing, China

JUAN FENG AND FEI XIE

College of Global Change and Earth System Science, Beijing Normal University, and State Key Laboratory of Numerical Modeling for Atmospheric Sciences and Geophysical Fluid Dynamics (LASG), Institute of Atmospheric Physics, Chinese Academy of Sciences, Beijing, China

(Manuscript received 23 May 2014, in final form 18 October 2014)

ABSTRACT

The time series of twentieth-century subtropical eastern Australian rainfall (SEAR) shows evident fluctuations over decadal to multidecadal time scales. Using observations from the period 1900–2013, it was found that SEAR is connected to the North Atlantic Oscillation (NAO) over decadal time scales, with the NAO leading by around 15 yr. The physical mechanism underlying this relationship was investigated. The NAO can have a delayed impact on sea surface temperature (SST) fluctuations in the subpolar Southern Ocean (SO), and these SST changes could in turn contribute to the decadal variability in SEAR through their impacts on the Southern Hemisphere atmospheric circulation. This observed lead of the NAO relative to SO SST and the interhemispheric SST seesaw mechanism are reasonably reproduced in a long-term control simulation of an ocean–atmosphere coupled model. The NAO exerts a delayed effect on the variation of Atlantic meridional overturning circulation that further induces seesaw SST anomalies in the subpolar North Atlantic and SO. With evidence that the NAO precedes SEAR decadal variability via a delayed SO bridge, a linear model for SEAR decadal variability was developed by combination of the NAO and Pacific decadal oscillation (PDO). The observed SEAR decadal variability is considerably well simulated by the linear model, and the relationship between the simulation and observation is stable. SEAR over the coming decade may increase slightly, because of the recent NAO weakening and the return of negative PDO phase.

1. Introduction

Subtropical eastern Australia (SEA; south of 25°S and east of 135°E), is a highly populated region and provides a large proportion of Australia's agricultural production. Thus, rainfall variability in this region has major implications for water resource management and has received a considerable amount of attention. Observations show that the subtropical Australian east coast experienced a drying trend during the second half of the twentieth century (Speer et al. 2011; Timbal and Fawcett 2013). Several studies have described the continuous drying across most of SEA and its impacts; of particular concern is the increasing strain on water resource availability (Murphy and Timbal 2008, and references therein). Therefore, an improved understanding of the causes of rainfall variability will assist future investigation of climatic variations and the associated high economic and societal significance.

The relationship between rainfall over Australia and large-scale climate variability has been investigated in

Corresponding author address: Jianping Li, College of Global Change and Earth System Science (GCESS), Beijing Normal University, Beijing 100875, China.
E-mail: ljp@bnu.edu.cn

DOI: 10.1175/JCLI-D-14-00372.1

various studies. Over interannual time scales, the El Niño–Southern Oscillation (ENSO) phenomenon acts as a primary driver of subtropical eastern Australian rainfall (SEAR; McBride and Nicholls 1983; Taschetto and England 2009). The SEA region tends to experience drought during El Niño events (warming in the eastern tropical Pacific), while La Niña events (cooling in the eastern tropical Pacific) are typically associated with increased rainfall over SEA. Recent studies have emphasized the impacts of the tropical Indian Ocean on SEAR variations. The Indian Ocean dipole (IOD), which is one of the leading modes of sea surface temperature (SST) variability in the tropical Indian Ocean (Saji et al. 1999), contributes to rainfall variability over southern and southeast Australia in the austral winter and spring seasons (Ummenhofer et al. 2009a,b; Cai et al. 2014). Although both ENSO and the IOD play an important role in modulating the interannual variability of SEAR, several studies have suggested that the mechanisms associated with these two modes are different (Cai et al. 2011). In addition to the effects of the tropical oceans, large-scale atmospheric circulation patterns in the Southern Hemisphere (SH) have also been suggested as plausible drivers of the climate in SEA. The southern annular mode (SAM; Thompson and Wallace 2000), which is defined as the leading mode of variability in the SH extratropical circulation, is thought to account for a large proportion of rainfall variability over southeast Australian coastal regions with an opposing influence in winter to that in spring (Meneghini et al. 2007; Hendon et al. 2007; Risbey et al. 2009; Cowan et al. 2013; Cai et al. 2014).

The influence of the interdecadal Pacific oscillation (IPO) on Australian rainfall over decadal time scales has been discussed in the literature. The IPO is used to describe the Pacific-wide ENSO-like pattern that can be obtained from empirical orthogonal function (EOF) analysis of global low-pass-filtered SST data (Parker et al. 2007). Previous studies have suggested that the IPO may be a Pacific-wide manifestation of the Pacific decadal oscillation (PDO; Mantua et al. 1997) and both correspond to the same physical phenomenon (Mantua and Hare 2002). The PDO shows fluctuations over decadal to multidecadal time scales and its phases are in good agreement with a number of climate indices around the Pacific (Mantua and Hare 2002). Previous studies have reported a statistical linkage between the PDO and eastern Australian rainfall over decadal time scales (Latif et al. 1997; Power et al. 1999a). In particular, above (below) average rainfall occurs over a large part of eastern Australia during the negative (positive) phase of the PDO. Cai et al. (2010b) have suggested that when the PDO is positive there is a tendency for the La Niña–rainfall teleconnection to break down, particularly over the SEA. Several studies have also shown that the two phases of the PDO strongly modulate year-to-year ENSO–rainfall variability over SEA. The ENSO–rainfall teleconnection appeared to be relatively strong from the mid-1940s to the late 1970s when the PDO was negative, while the ENSO–rainfall teleconnection was significantly weaker before the mid-1940s and after 1980, when the PDO was positive (Power et al. 1999b, 2006).

The North Atlantic Ocean also features remarkable variability over decadal to multidecadal time scales, which has received a considerable amount of attention as it offers a potentially large source of predictability of natural climate variability (Delworth and Mann 2000; Latif et al. 2006a,b). The principle expression of this variability is the oscillation of North Atlantic SST between alternating warm and cold phases, which has been commonly referred to as the Atlantic multidecadal variability (AMV; Enfield et al. 2001; Zhang et al. 2013). For the atmospheric circulation, the North Atlantic Oscillation (NAO) is the dominant mode of atmospheric variability over the North Atlantic region (Hurrell 1995), and it displays fluctuations over multiple time scales ranging from interannual to multidecadal (Wanner et al. 2001). The NAO is a seesaw pattern in surface pressure, with coherent changes over the high and midlatitudes. A negative (positive) NAO indicates weakening (strengthening) of both the Icelandic low and Azores high, which results in a decreased (increased) sea level pressure (SLP) gradient across the North Atlantic region and further reduces (enhances) the strength of the westerlies (Li and Wang 2003; Wu et al. 2009). Previous studies have also suggested that the NAO variability significantly influences oceanic variability in the North Atlantic, such as the SST tripole pattern and the strength of the ocean circulation (Visbeck et al. 2003, and references therein; Wu et al. 2009, 2012). Recent studies have shown that the NAO plays an important role in the AMV and contributes significantly to the decadal predictability of the Northern Hemisphere (NH) climate (Latif et al. 2006a,b; Latif and Keenlyside 2011; Li et al. 2013).

So far, there have been few studies linking the climate over Australia to variability in the North Atlantic region. Cai and Cowan (2007) provided a modeling analysis to show that increasing NH aerosols potentially mitigate the slowdown of the Atlantic meridional overturning circulation (AMOC) and further lead to the rainfall changes in southern Australia. However, the SH climate response to aerosols is model dependent because of large uncertainties in the representation of aerosol-related physics. Thus, it remains unclear whether the NAO or AMV can affect Australian rainfall over decadal to multidecadal time scales. If it does, how

are they related and what is the underlying mechanism? In this paper, we attempt to address these questions. The present study presents evidence that the NAO can influence SST fluctuations in the Southern Ocean (SO) and that these SST changes could in turn contribute to the decadal variability in SEAR through their impacts on the SH atmospheric circulation.

The remainder of this manuscript is organized as follows: The datasets and methodology are described in section 2. The statistical relationships among the NAO, SO SSTs, and SEAR are described in section 3. Section 4 demonstrates the relationship using coupled model simulations and explores the underlying mechanism. In section 5, an empirical model is established to explain the decadal variability of SEAR based on the NAO and PDO. Finally, conclusions and a discussion are presented in section 6.

2. Data and methodology

a. Data

Monthly observed rainfall data for the Australian continent (available for the period 1900–2013) on a 0.05° latitude/longitude grid were used in this study (Jones et al. 2009). The following three sets of monthly precipitation data were also employed: 1) the dataset constructed by the Climate Research Unit (CRU; Harris et al. 2014), where the CRU data are available on a resolution of 2.5° × 2.5° grid for the period 1901–2009; 2) precipitation data developed by the Global Precipitation Climatology Centre full data reanalysis version 6.0 (GPCC v6) with a resolution of 2.5° × 2.5° grid for the period 1901–2010 (Schneider et al. 2011); and 3) Global Historical Climatology Network (GHCN) version 2 with a resolution of 5° latitude/longitude grid for the period 1900–2010. To compare the results among different datasets and to focus on relatively large-scale variability in the rainfall, the BoM precipitation data were regridded onto a coarser resolution (2° latitude/longitude) using the distance-weighted averaging interpolation method. As the results from all four datasets were similar, here we show only the results based on the BoM precipitation data unless specified otherwise.

Two sets of global monthly surface temperature anomalies were obtained from the Goddard Institute for Space Studies (GISS; Hansen et al. 2010, and references therein) and the National Climatic Data Centre (NCDC; Smith et al. 2008) for the analysis period 1900–2013. The observational global SST data derived from the extended reconstruction SST version 3 (ERSST v3b) dataset (Smith and Reynolds 2005) were also employed to test the reliability of the results. Results from the two surface temperature datasets were similar to the ERSST data, and thus we show only the results from the NCDC data unless specified otherwise. Atmospheric data available for the period 1900–2012 were obtained from NOAA's Twentieth Century Reanalysis (Compo et al. 2011) including wind fields and precipitable water (vertically integrated specific humidity), and the SLP field was derived from the Hadley SLP dataset (Allan and Ansell 2006). The observed NAO index used in this study is defined as the difference in the normalized SLP zonally averaged over the North Atlantic sector from 80°W to 30°E between 35° and 65°N (Li and Wang 2003; Li 2005; Li et al. 2013; Wu et al. 2011) and was derived from the NCAR SLP dataset available during 1900–2013 (Trenberth and Paolino 1980). The PDO index was obtained from the University of Washington (http://jisao.washington.edu/pdo/PDO.latest). Details of this index can be found in Mantua et al. (1997).

Global ocean reanalysis data are relatively short and there is still large uncertainty in the reanalysis products regarding the subsurface ocean long-term variability: for example, variations in AMOC (Tett et al. 2014). Climate models provide a useful approach to the analysis of multidecadal variability. A long-term simulation by the Community Climate System Model, version 4 (CCSM4) was used here, specifically a 500-yr-long segment of a preindustrial control run. The CCSM4 is a fully coupled model of earth's physical climate system; a general description of this model may be found in Gent et al. (2011). Several recent studies have used the CCSM4 preindustrial control simulations to investigate the AMV and found that the CCSM4 captures this variability reasonably well and that the model does not exhibit significant climate drift in the long-term simulations (Danabasoglu et al. 2012; Zanchettin et al. 2014). The CCSM4 simulation data used in our analysis included variables from the air–sea interface (e.g., SLP and SST), as well as variables from the deep ocean (e.g., AMOC).

b. Statistical methods

The statistical significance of the linear regression coefficient and correlation between two autocorrelated time series is accessed via a two-tailed Student's t test using the effective number of degrees of freedom (Pyper and Peterman 1998; Li et al. 2013; Li et al. 2012; Xie et al. 2014). The effective number of degrees of freedom N^{eff} is given by the following approximation:

$$\frac{1}{N^{\text{eff}}} \approx \frac{1}{N} + \frac{2}{N}\sum_{j=1}^{N}\frac{N-j}{N}\rho_{XX}(j)\rho_{YY}(j), \qquad (1)$$

where N is the sample size and $\rho_{XX}(j)$ and $\rho_{YY}(j)$ are the autocorrelations of two sampled time series X and Y at time lag j.

The confidence intervals for values predicted by the linear regression (von Storch and Zwiers 1999) are determined from

$$\hat{y}_i \pm t_{(1+p)/2}\sigma\sqrt{1+\mathbf{x}_i^{\mathrm{T}}(\mathbf{X}^{\mathrm{T}}\mathbf{X})^{-1}\mathbf{x}_i}, \qquad (2)$$

where $\hat{y}_i$ represents the predicted value corresponding to the ith realization of the predictor variables, $\mathbf{x}_i$ is the vector of predictor variables for the ith realization, and $\mathbf{X}$ is the design matrix of predictor variables for different realizations. The quantity σ is the root-mean-square error of the fitted and observed values of the dependent variable y, and $t_{(1+p)/2}$ is the appropriate quantile of the t distribution with $(n-k-1)$ degrees of freedom, where n and k are the number of realizations and predictor variables, respectively, and p is the confidence level (here, $p = 0.95$).

c. AGCM model

We also performed idealized numerical experiments to investigate the atmospheric circulation response to a certain SST pattern. All experiments were designed and implemented on the Simplified Parameterizations, Primitive Equation Dynamics (SPEEDY) model developed at the Abdus Salam International Centre for Theoretical Physics (Kucharski et al. 2013). SPEEDY is an intermediate complexity AGCM based on a spectral primitive equation dynamical core with a hydrostatic, sigma coordinate, spectral transform, and semi-implicit treatment of gravity waves. The resolution used here is triangular 30 (T30; i.e., ~3.75° × ~3.75° horizontal resolution), with eight vertical levels. The model includes physically based parameterizations of shallow and deep convection, large-scale condensation, clouds, shortwave and longwave radiation, vertical diffusion, and surface momentum and energy fluxes. The model is computationally inexpensive, due to the simplified parameterizations, as well as the relatively low horizontal and vertical resolutions. Nevertheless, the simulation performance of the SPEEDY model compares very well with that of more complex AGCMs with respect to extratropical large-scale variability (Kucharski et al. 2013, and references therein).

3. Observational evidence for the NAO impact on SEAR

Figure 1 shows the 11-yr running means (here corresponding to decadal time scales) of annual (January–December)-mean NAO index and SEAR anomalies for the period of 1900–2013. Throughout the whole period, the NAO fluctuates between positive and negative phases with time scales of the order of decades, and no significant trend is found. The SEAR index was calculated as the area-weighted average of annual-mean land precipitation anomalies over continental Australia south of 25°S and east of 135°E. The SEAR indices from four different datasets (BoM, CRU, GPCC, and GHCN) are highly correlated over the common overlap period (not shown here), indicating that the temporal features of SEAR are broadly consistent in all the datasets. The SEAR index shows no statistically significant trend for the whole period 1900–2013. It can be seen from Fig. 1a that the annual-mean NAO and SEAR show pronounced decadal to multidecadal variability and a phase lag of about 10–20 yr (SEAR lagging NAO). For example, the decline in the NAO between the 1920s and 1960s was followed by the wetting of SEA about 15 yr later; furthermore, the strengthening of the NAO between the 1960s and 1990s led the drying of SEA by around 10 yr.

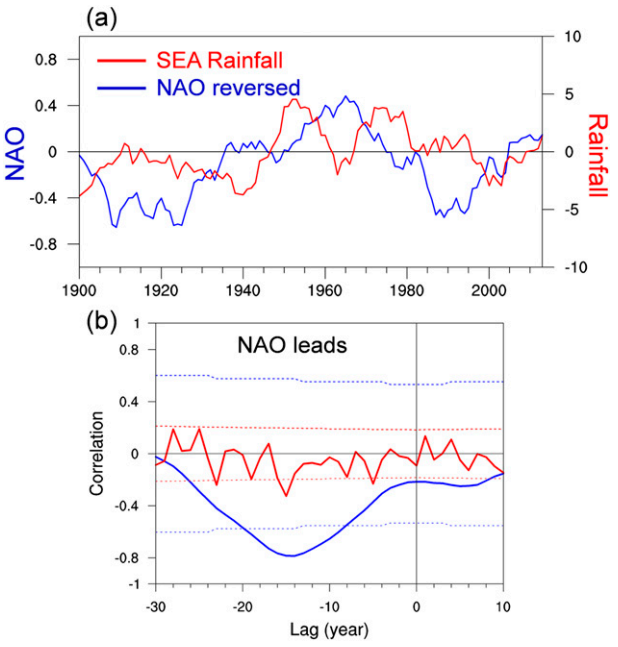

FIG. 1. (a) Observed decadal time series of the annual-mean NAO index and SEAR anomalies (mm month^{-1}) for the period 1900–2013. For ease of comparison, the sign of the NAO index has been reversed. (b) Lead–lag correlation between the annual-mean NAO and SEAR indices (1900–2013). The red (blue) line is the annual-mean (decadally smoothed) time series. Negative (positive) lags indicate that the NAO is leading (lagging), and the red (blue) dashed lines are the 95% confidence levels for the unsmoothed (smoothed) time series based on the effective numbers of degrees of freedom.

Figure 1b shows the lead–lag correlations between the annual-mean NAO and SEAR indices based on both unfiltered and decadally smoothed data. Consistent with the discussion above, the maximum correlation coefficients (−0.37 for unfiltered data and −0.79 for the

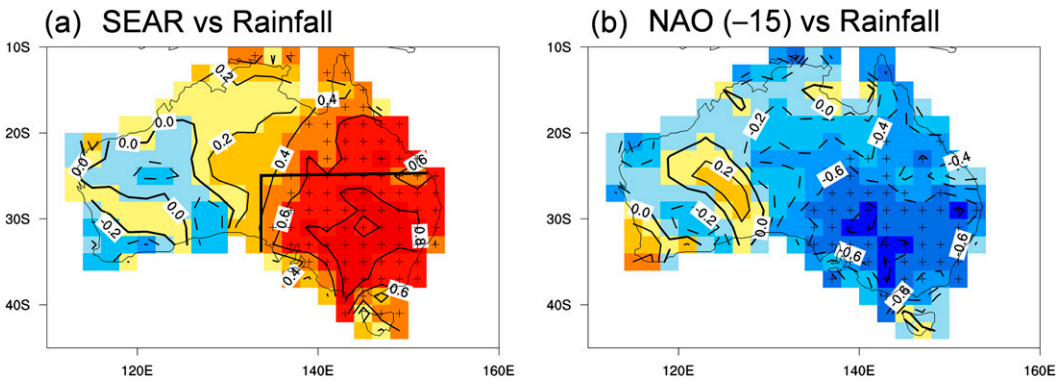

FIG. 2. (a) Correlation map between the annual-mean SEAR index and Australian precipitation over decadal time scales for the period 1900–2013. The two black perpendicular lines indicate the northern and western boundaries of the SEA region (continental Australia south of 25°S and east of 135°E), where the SEAR index is defined. (b) Lagged correlation between the annual-mean precipitation and the NAO over decadal time scales for 1900–2013, with the NAO leading by 15 yr. Warm (cold) colors in (a),(b) represent positive (negative) correlation coefficients, and the color shading interval is 0.2, the same as the contour interval. The areas marked by + signs in (a),(b) are significant above the 95% confidence level.

smoothed data, both significant at the 95% confidence level) occur at a lag of approximately 15 yr (NAO leading SEAR); the simultaneous correlations are near 0, and no significant correlations are found when SEAR leads the NAO. Note that, for comparison, the sign of the NAO index is reversed in Fig. 1a. This suggests that the positive (negative) NAO phase precedes the SEA dry (wet) condition and can be considered to be a precursor to the decadal variability of SEAR. Moreover, the relationship between the SEAR and 15-yr-ahead NAO is basically symmetrical about positive and negative NAO phases. For positive (negative) NAO phases, the correlation between the SEAR and 15-yr-ahead NAO is −0.80 (−0.71), significant at the 95% confidence level. Thus, the influence of NAO on the SEAR is apparent during both phases of the NAO. The spatial pattern of SEAR decadal variability is shown in Fig. 2a and exhibits high correlations of the same sign over most of SEA. Figure 2b shows the lagged correlation pattern of the decadal land precipitation with respect to the NAO (NAO leads by 15 yr). The correlations between Australian land precipitation and the NAO index 15 yr earlier are significantly negative and have a homogeneous pattern over the SEA region that resembles the spatial pattern of SEAR decadal variability (as shown in Fig. 2a). Thus, these results, a decadal time scale, indicate that the atmospheric seesaw pattern in the North Atlantic leads the dry/wet conditions in SEA by around 15 yr.

Large-scale SST variability can have a significant influence on regional climate, as the ocean is the memory of the climate system, particularly over decadal time scales. It is known that the surface temperature warming trend is related to the increase in greenhouse gas concentrations during the twentieth century. This influence needs to be carefully filtered when focusing on decadal or multidecadal variability. Previous studies have removed a linear (Zhang et al. 2007) or a quadratic (Enfield and Cid-Serrano 2010) trend to retrieve the low-frequency variability. In this study, the linear trend was removed from the surface temperature datasets over the period 1900–2013 prior to analysis. In fact, removing a second order polynomial gives qualitatively similar results. Figure 3 shows the correlation pattern between the SH SST anomalies and SEAR over decadal time scales. Significantly positive correlations occur within the 65°–45°S band in the SO, to the south of Australia. Moreover, the correlation pattern mainly features a zonally symmetric annular structure in terms of the zonal-mean profile and horizontal distribution, although the positive correlations over the south Indian and South Atlantic basins are most pronounced. To quantitatively describe such an SST belt in the SO, we derived the SO SST index (SOSSTI) as the area-weighted average of the detrended SST anomalies within the latitude band 65°–45°S. A high simultaneous correlation coefficient (r = 0.70, significant at the 95% confidence level) is observed between the SEAR index and SOSSTI based on the decadally smoothed data (1900–2013), indicating that the SST variations over the high-latitude SO are closely associated with SEAR decadal variability.

The lagged correlation pattern of decadal SH SST with respect to the NAO (NAO leads by 15 yr) is shown in Fig. 3b. The correlations of the SST with the NAO at a lag of 15 yr are statistically significant within the latitude band 65°–45°S over the SO, and the corresponding zonal-mean profile also shows significant correlations of the same sign south of 45°S. The lagged correlation between the NAO and SOSSTI (Fig. 4) also shows a remarkable correlation peak (−0.36 for the unfiltered data

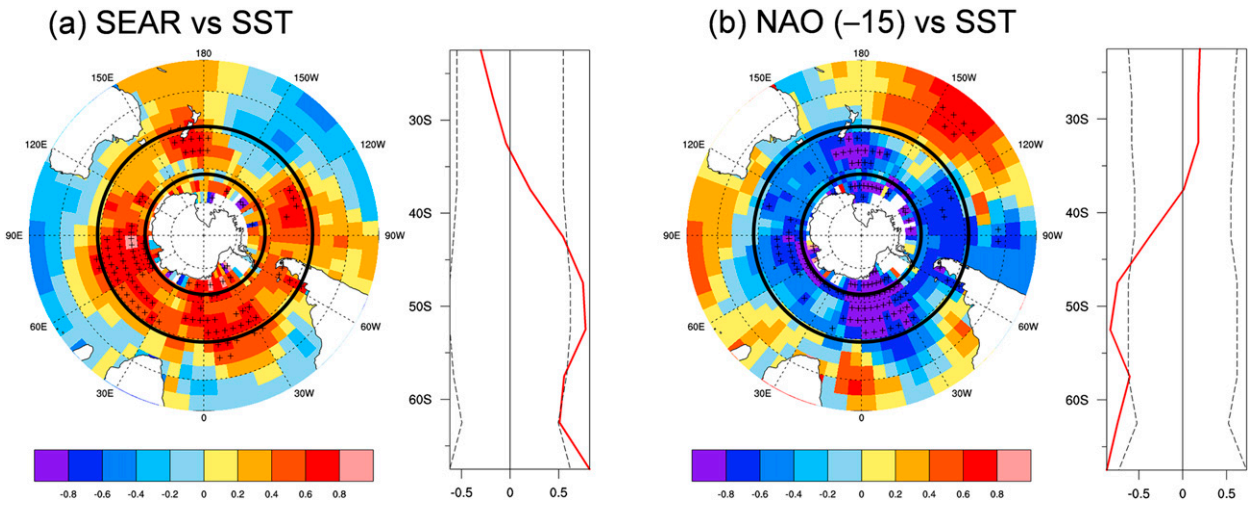

FIG. 3. (a) Correlation between the annual-mean SEAR index and SH SST (south of 20°S) over decadal time scales for the period 1900–2013. Correlations for the zonal-mean temperature are shown as a red line, and the black dashed lines denote the 95% confidence level. (b) Lagged correlation between the annual-mean SH SST and the NAO over decadal time scales for 1900–2013, with the NAO leading by 15 yr. Lagged correlations for the zonal-mean temperature are shown as a red line, and the black dashed lines denote the 95% confidence level. The areas marked by + signs in (a),(b) are significant above the 95% confidence level, and the two black circles indicate the 45° and 65°S circles. The long-term linear trend in temperature data since 1900 was removed prior to the correlation analysis.

and −0.78 for the smoothed data, both significant at the 95% confidence level) around lag −15 yr (NAO leads), further demonstrating that the NAO may lead decadal variations of the high-latitude SO SST. On the other hand, the above analysis suggests an in-phase relationship between SO SST and SEAR at decadal time scales. We hypothesize that two mechanisms are involved in the communication between the North Atlantic and Australia: One is that the NAO may have a delayed effect on high-latitude SO SST through oceanic processes, and the other is that the SO SST may in turn exert an impact on SEAR through changes in the SH atmospheric circulation. Thus, the high-latitude SO may act as a critical bridge in the teleconnection between the NAO and SEAR.

To better understand the bridging role of SO SST, we first investigated the mechanisms involved in the link between SO SST and SEAR over decadal time scales. Before examining rainfall variations, we will discuss the atmospheric properties of mean states in the SH. As shown in Fig. 5a, long-term annual-mean atmospheric precipitable water shows a remarkable moisture contrast between land and ocean, with wetter conditions over the ocean. This gives rise to an eastward moisture gradient over the subtropical Australian east coast. In addition, the zero-wind line (interface between low-level easterly and westerly winds) is located around 30°S throughout the subtropical Australian continent. Figure 5b presents the composite differences of atmospheric precipitable water and low-level (700–850-hPa average) winds between high and low SEAR years. The contrasting positive and negative anomalies in eastern and western Australia, respectively, are observed in the precipitable water field, featuring an east–west dipole structure. This zonally asymmetric structure may be related to the low-level zonal wind, which affects the zonal transport of moisture. The low-level winds mainly show a belt of easterly anomalies between 40° and 20°S, with two centers of action located over the subtropical Australian east coast and the west coast of South America. A recent observational study has also reported a close linkage between the SH midlatitude zonal wind and eastern Australian rainfall at decadal time scales and showed that the zonal wind change is critical for moisture transport across eastern Australia (Rakich et al. 2008).

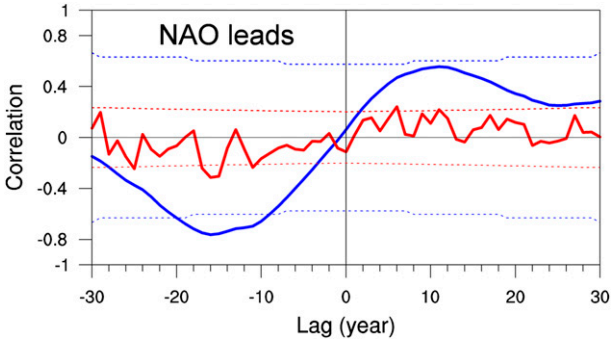

FIG. 4. As in Fig. 1b, but for the annual NAO and SOSSTI. Note that the long-term linear trend in temperature data since 1900 was removed prior to the correlation analysis.

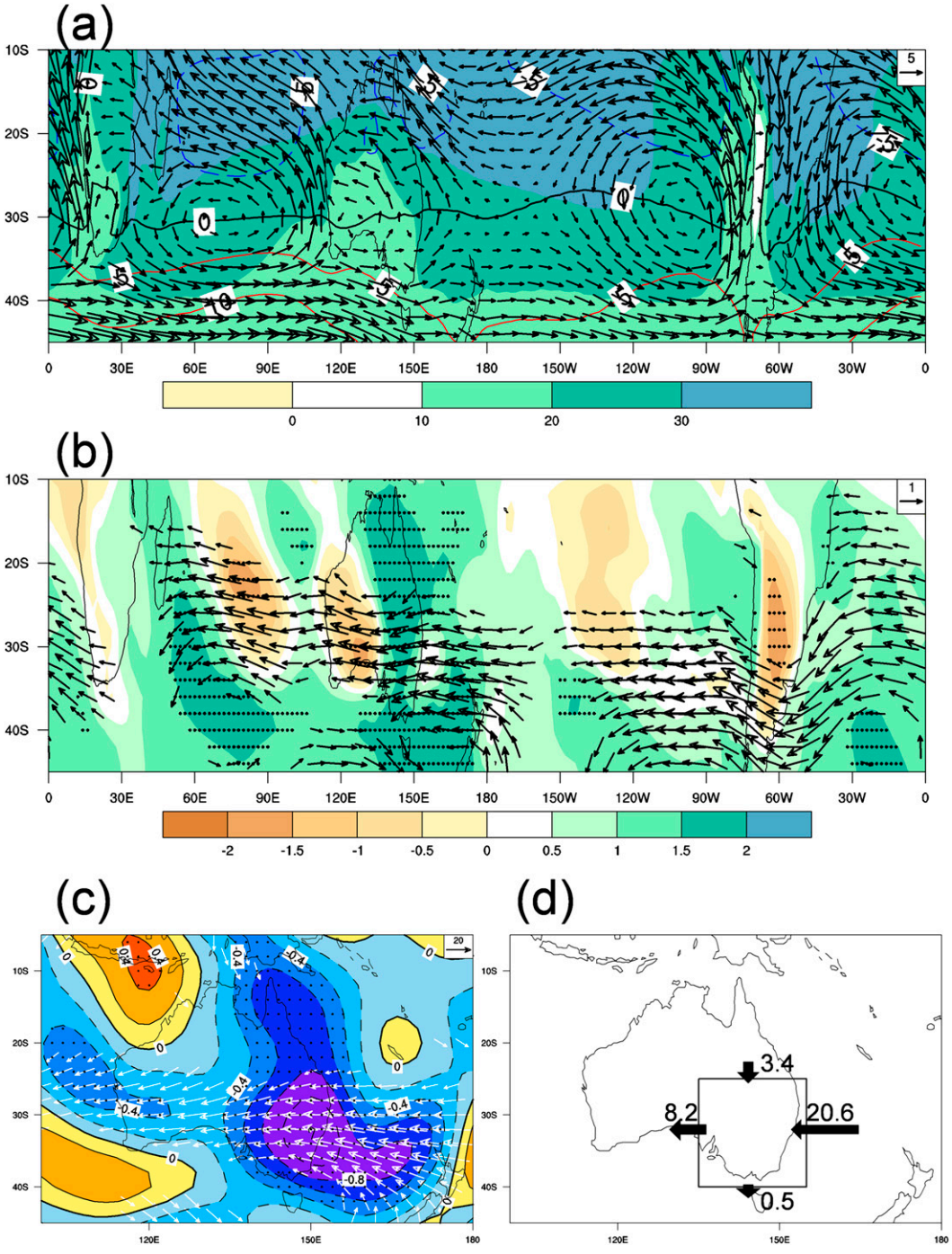

FIG. 5. (a) Long-term mean background states of atmospheric precipitable water (shaded; kg m^{-2}), low-level (700–850-hPa average) zonal wind (contours; m s^{-1}), and low-level winds (vector) in the SH. (b) Composite differences of precipitable water (shaded) and low-level winds (vectors) between high and low SEAR years. The high (low) SEAR years are selected with the decadal SEAR greater than one positive (negative) standard deviation of the index. The values in the dotted areas are significant at the 95% confidence level of the *t* test for the precipitable water field; only the vectors significant at the 95% confidence level are given. (c) As in (b), but for the vertically integrated moisture flux (vectors; Kg m^{-1} s^{-1}) and moisture divergence (shaded; 10^{-5} Kg m^{-2} s^{-1}). (d) Composite differences of zonal and meridional moisture fluxes passing across the boundaries of the box covering SEA (40°–25°S, 135°–155°E) between high and low SEAR years. The dark arrows indicate the positive direction of flux across each boundary.

As the maritime air masses always contain more moisture than the continental ones, the easterlies can result in a westward moisture transport near the Australian east coast and so increase the moisture supply there.

To gain further insights into the potential moisture source associated with SEAR decadal variability, we also examined moisture transport. Figure 5c shows the composite difference in vertically integrated (1000–400 hPa) moisture flux anomalies and its divergence for high minus low SEAR years. The vertically integrated moisture flux was calculated according to Nnamchi and Li (2011) and Nnamchi et al. (2013). The moisture flux is generally zonally directed between 40° and 20°S during the high SEAR years and shows strong westward moisture advection across the SEA region reminiscent of the anomalous easterlies in the lower troposphere. Strong moisture convergence anomalies occur over the subtropical Australian east coast and correspond closely to the precipitation increase. The zonal and meridional moisture fluxes passing across the boundaries of the box covering SEA were analyzed further. As shown in Fig. 5d, during the high SEAR years, the strongest moisture flux originates from the South Pacific, with moisture being transported westward, and as a result the easterly moisture flux across the eastern boundary contributes most to the moisture convergence. Therefore, the anomalous easterlies between 40° and 20°S intensify the easterly moisture transport to the SEA region, provide the moisture source for moisture flux convergence, and consequently lead to the significant increases in precipitation.

The wind vectors (Fig. 5b) and moisture fluxes (Fig. 5c) also suggest the presence of an anomalous anticyclone (high pressure cell) to the south of Australia, allowing moist easterlies to penetrate eastern Australia. Cowan et al. (2013) suggested that this anticyclone is strongly coherent with positive blocking events at 130°–140°E and therefore provides large rainfall totals to the southeast Australia. Given the strong coherence between the anomalous anticyclone and the blocking highs (Cowan et al. 2013), a simple index reflecting the variation of the blockings could be defined as the area-weighted average of SLP over the region 45°–55°S, 150°E–170°W. This blocking high index is positively correlated with the SEAR over decadal time scales (r = 0.68, significant at the 95% confidence level), confirming the strong association of SEAR to the blocking events (Risbey et al. 2009).

It is known that the meridional temperature gradient is able to modulate the strength of the zonal wind as a consequence of thermal wind balance. Figure 6a shows time series of low-level zonal wind averaged between 40° and 20°S, the meridional SST gradient in the SO (30°–10°S average minus 65°–45°S average), and the SOSSTI. It is found that the decadal variability of the SST gradient can be largely explained by the SOSSTI ($r = -0.87$, significant at the 95% confidence level) and that the zonal wind change is coherent with the meridional SST gradient ($r = 0.78$). Thus, a significant antiphase relationship is observed between the zonal wind index and the SOSSTI ($r = -0.70$). Moreover, the blocking high index is significantly correlated with the meridional SST gradient ($r = -0.69$) and SOSSTI (r = 0.64) over decadal time scales, respectively. This indicates that the decadal variation in the blocking highs is also related to the meridional SST gradient, further providing a dynamical link between extratropical SO SSTs and the SEAR.

Previous modeling studies have suggested a connection between the extratropical meridional temperature gradient and SAM variability (e.g., Cai et al. 2010a). We also investigated the role of SAM variability in the link between SO SSTs and the SEAR. A positive correlation ($r = 0.47$) is observed between the meridional SST gradient and the annual-mean SAM index (reconstructed by using principal component regression and available for the period 1905–2005; Fogt et al. 2009) over decadal time scales. However, the correlation between the annual-mean SAM and SEAR over decadal time scales is low and insignificant ($r = -0.31$). In addition, the correlations between the decadal-scale meridional SST gradient and SEAR before and after removal of the SAM signal are −0.80 and −0.77 (both significant at the 95% confidence level), respectively. This indicates that the link between extratropical SO SSTs and the SEAR over decadal time scales is robust and independent of the SAM variability.

To further demonstrate the influence of high-latitude SO SST anomalies on the wind field and rainfall, we performed numerical experiments using the SPEEDY model described in section 2. The control run was integrated for 15 yr and forced with the climatological SST, and the last 10 yr of the integrations were used to provide the basic annual-mean state. The sensitivity experiment was integrated for 12 yr, and a 10-member ensemble mean was constructed from the last 10 yr of the integrations to reduce the uncertainties arising from different initial conditions. To isolate and mimic the impact of SST variations on atmospheric circulation, the only difference between the sensitivity and control experiments was a 1°C increase in SST over the 65°–45°S region in the sensitivity run. Figure 6b shows that warm SST anomalies south of 45°S excite anomalous easterlies north of 45°S and induce an anomalous anticyclone (high pressure cell) south of Australia, consistent with

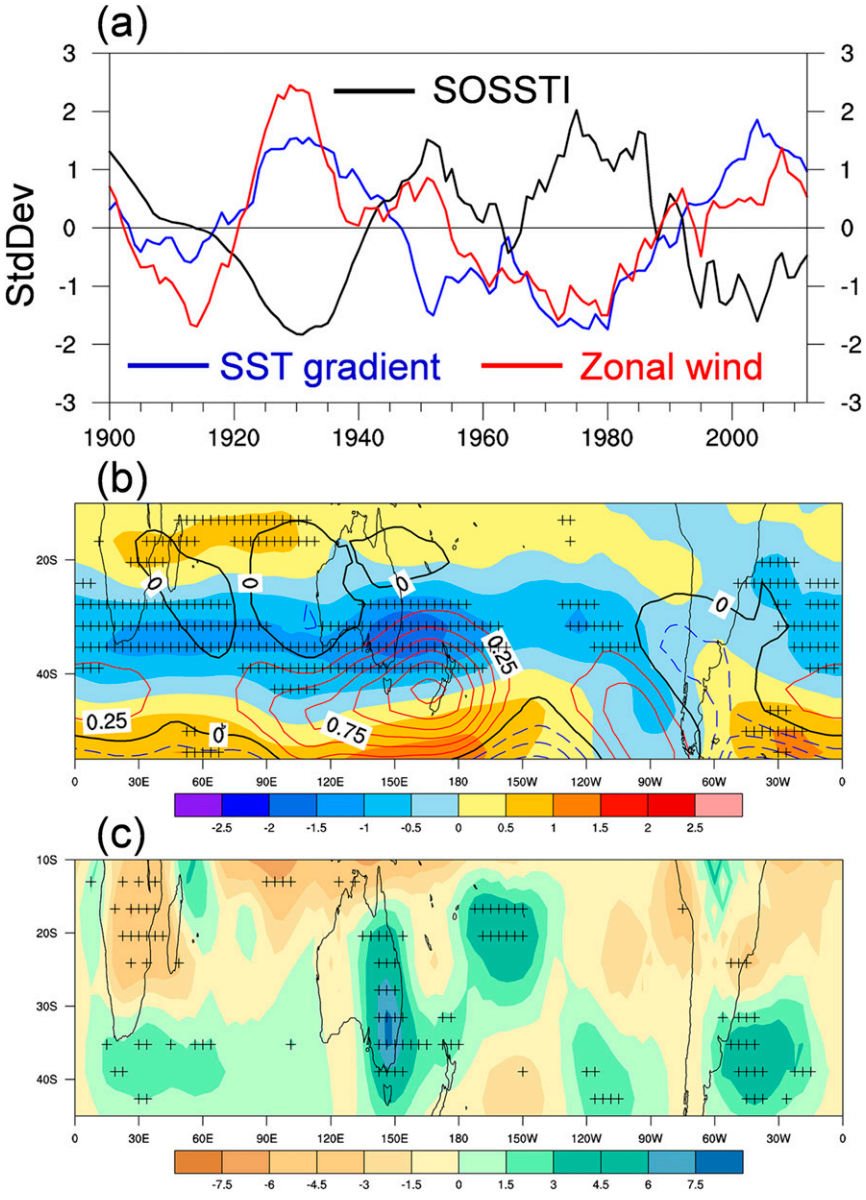

FIG. 6. (a) The 11-yr running mean time series of low-level zonal wind averaged between 40° and 20°S, meridional SST gradient in the SO (30°–10°S average minus 65°–45°S average), and the SOSSTI for 1900–2012. The three indices are normalized by the long-term standard deviation. (b) Simulated SH low-level zonal wind (shaded; m s^{-1}) and SLP (contours; hPa) in response to warm SST anomalies over high-latitude SO in the SPEEDY model. The + signs indicate the regions where the results from the sensitivity simulations are significantly different from the control at the 95% confidence level for the zonal wind (Student's *t* test). (c) As in (b), but for the SPEEDY simulated rainfall (mm month^{-1}).

the observed response. The simulated zonal wind response to the high-latitude SO warming largely resembles the wind pattern associated with SEAR decadal variability, particularly for the center of action near the Australian east coast. Figure 6c further displays the simulated rainfall in response to the SO SST warming, which shows anomalously wet conditions in the SEA region. Thus, we have provided modeling evidence for the physical mechanism associated with the in-phase relationship between SO SST and SEAR. In the following section, we focus on testing the hypothesis that the NAO has a delayed impact on high-latitude SO SST.

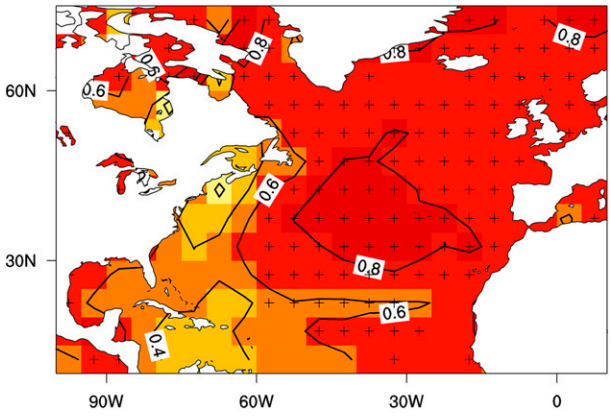

FIG. 7. Lagged correlation between annual-mean North Atlantic SST anomalies and the NAO index over decadal time scales for 1900–2013 with the NAO leading by 15 yr. The long-term linear trend in temperature since 1900 was removed prior to the correlation analysis. Warm colors represent positive correlation coefficients, and the color shading interval is 0.2, the same as the contour interval. The areas marked by + signs are significant above the 95% confidence level.

4. Delayed influence of the NAO on SO SST

The delayed effect of the NAO decadal variability on the North Atlantic Ocean has been discussed extensively in earlier numerical modeling studies (Visbeck et al. 1998; Delworth and Greatbatch 2000; Eden and Jung 2001; Eden and Greatbatch 2003). There is substantial modeling evidence that NAO-related surface turbulent heat flux and wind stress anomalies over the North Atlantic Ocean, particularly over the Labrador Sea, have an important impact on multidecadal fluctuations of the AMOC, which in turn produce the SST signatures of the AMV. Thus, the AMV may be a delayed response to NAO variability with a decadal-scale time lag (Visbeck et al. 1998; Delworth and Greatbatch 2000; Eden and Jung 2001). The NAO impact on the AMOC has also been demonstrated in observational studies, and the long-term change in the AMOC is thought to be related to the low-frequency variations of the NAO through changes in convection in the Labrador Sea (Latif et al. 2006a; Latif and Keenlyside 2011). Recently, Li et al. (2013) have further identified the lead time between the NAO and AMV over decadal time scales (15–20 yr) using observational data and applied this lead–lag relationship to the decadal prediction of the NH surface temperature. As shown in Fig. 7, the correlations between SSTs over the extratropical North Atlantic and the NAO 15 yr earlier are positive basinwide and statistically most significant over the northern North Atlantic (north of 40°N).

The variations of the AMOC not only affect the climate of the North Atlantic but also have a large effect on the SO. For example, modeling suggests that an AMOC collapse significantly reduces northward heat transport and yields a net transport of heat from the NH to the SH, which can thus induce an interhemispheric dipole pattern of northern cooling and southern warming of surface temperatures (Zhang and Delworth 2005; Stouffer et al. 2006; Chiang and Friedman 2012; Danabasoglu et al. 2012). The AMOC-forced dipole pattern shows the largest amplitudes of opposite signs over the subpolar North Atlantic and Antarctic Circumpolar Current region and is often regarded as internal climate variability (Yang et al. 2013; Wang et al. 2014). Consequently, an SST dipole index has been defined and is used as an indicator of AMOC variations (Latif et al. 2006a). Paleoclimate records and simulations also suggest a bipolar seesaw pattern in surface temperature that shows an antiphase relationship between northern North Atlantic and high-latitude SO SSTs (Stocker and Johnsen 2003; Knutti et al. 2004). Recent studies using long-term observations have further confirmed the interhemispheric SST seesaw and revealed the north–south climate connection over multidecadal time scales (Latif et al. 2006a; Chylek et al. 2010; Dima and Lohmann 2010; Sun et al. 2013; Latif et al. 2013). Although these studies were based on either different sets of surface temperature data or different statistical methods, there is some consensus that the interhemispheric SST seesaw is most pronounced in the subpolar regions of the North Atlantic and SO. Thus, in light of these findings, the SST variations in these two key regions may be physically connected, and it is possible that this subpolar interhemispheric SST seesaw mechanism is responsible for the lead of the NAO relative to the SO SST.

Figure 8a shows the correlation between SH temperature and the SST average for the northern North Atlantic region (40°–70°N, 70°W–0°) over decadal time scales. Strong negative correlations are found within the latitude band 65°–45°S in the SO (also evident in the zonal-mean profile) and are most robust over the subpolar basins south of the South American continent. Moreover, the correlation between the SOSSTI and SST average for the northern North Atlantic is significantly negative ($r = -0.84$ for decadal time scales, significant at the 95% confidence level). This indicates that the SSTs in the subpolar SO are highly anticorrelated with those in the subpolar North Atlantic, which is basically consistent with the aforementioned subpolar interhemispheric seesaw pattern. To highlight the role of the interhemispheric SST seesaw mechanism in the NAO–SO connection, we repeated the correlation analysis shown in Fig. 3b but for the SH SST data after removing the effect of the subpolar interhemispheric SST seesaw (by subtracting the linear regression onto the northern North Atlantic SST from the temperature data). As shown in Fig. 8b, no statistically significant correlation is

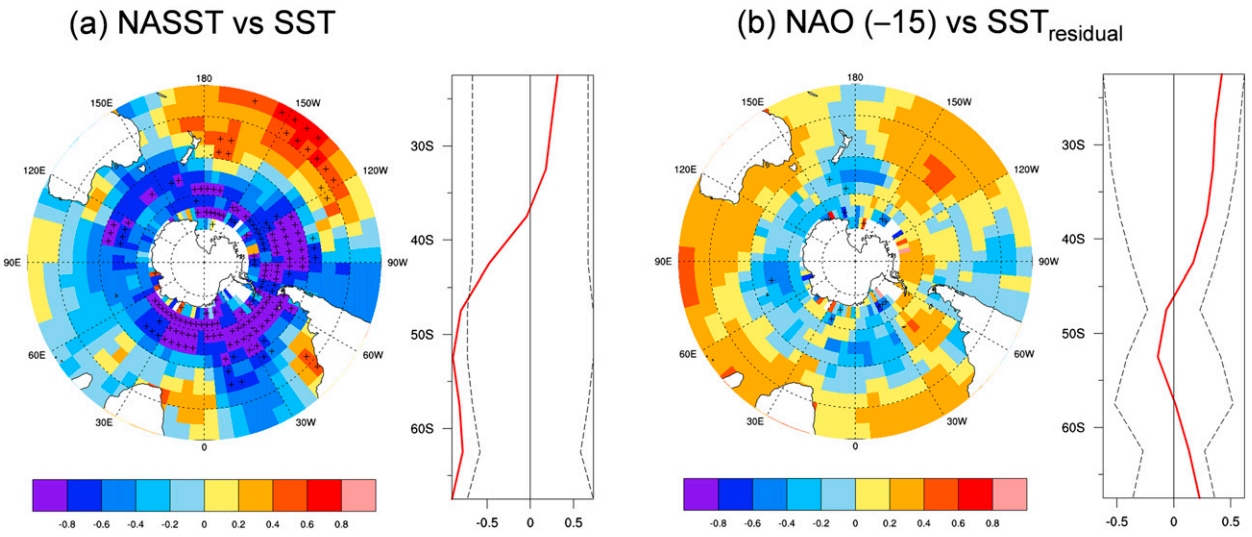

FIG. 8. The subpolar interhemispheric SST seesaw effect. (a) As in Fig. 3a, but for the correlations with the SST average over the northern North Atlantic (40°–70°N, 70°W–0°). (b) As in Fig. 3b, but for the temperature data after removing the effect of the subpolar interhemispheric SST seesaw (by subtracting the regression onto the northern North Atlantic SST from the temperature data).

found in the high-latitude SO, and the correlations for the zonal-mean temperatures are low and insignificant. Furthermore, the peak for the 15-yr lead correlation between the NAO and SOSSTI is no longer evident (not shown here). Therefore, according to the above results, the NAO leads the SO SST variations over decadal time scales possibly because of its delayed effect on the AMOC, which may be manifested by the subpolar interhemispheric SST seesaw.

Because of the paucity of historical observations from the deep ocean and large uncertainty in subsurface ocean reanalyses, we used long-term simulations from a state-of-the-art climate model (CCSM4) to provide further evidence that the NAO and SO SST are physically connected. The NAO index in CCSM4 is defined in a similar manner to that in the observations, and is highly correlated with the principal component (PC)-based index of the NAO, defined as the leading EOF of annual SLP anomalies over the North Atlantic sector (20°–80°N, 90°W–30°E), yielding a correlation coefficient of 0.92 for the entire simulation period. The lead–lag correlation between the SST average in the northern North Atlantic and the NAO index (red line in Fig. 9a) shows a maximum positive correlation coefficient ($r = 0.49$, significant at the 95% confidence level) at a lag of around one decade (NAO leads). A significantly negative correlation ($r = -0.42$) is also found when the NAO leads the SOSSTI (blue line in Fig. 9a), peaking at a lag of about 10 yr. In addition, the SST average in the northern North Atlantic is significantly anticorrelated with the SOSSTI over decadal time scales ($r = -0.52$), corresponding to the subpolar interhemispheric seesaw in the simulations. Thus, the relationships among the NAO, northern North Atlantic SST, and SO SST are very well simulated by the CCSM4, although the time for the lead of NAO to the temperatures is slightly shorter than in the observations. Figure 9b further shows the lagged correlation map of global SSTs with the NAO index, calculated with the NAO index leading by 10 yr. In the North Atlantic, the correlation map is characterized by positive values across most of the basin, with the highest correlations in the subpolar gyre region. Conversely, correlations are generally negative in the high-latitude band of the SO (65°–45°S), except for the offshore region east of the Antarctic continent, and most significant negative correlations are observed over the southern South Atlantic and the oceans south of South America and New Zealand. Similarly to the observational analysis, we calculated the lagged correlation between the NAO and SO SST (NAO leads by 10 yr) after removal of the subpolar interhemispheric SST seesaw effect and found no significant correlations in the high-latitude SO (not shown here). Therefore, the observed lead of the NAO compared to the SO SST and the interhemispheric SST seesaw effect are realistically reproduced in the control simulation with the CCSM4.

Previous model studies indicated that the surface temperature interhemispheric seesaw might be a consequence of the changes to the AMOC beneath the surface. The long-term mean streamfunction of AMOC for the CCSM4 simulation is shown in Fig. 10a. Based on the hydrographic data, estimates of the AMOC strength are 14–18 Sv ($1\ \text{Sv} \equiv 10^6\ \text{m}^{-3}\ \text{s}^{-1}$) at 24°N (Ganachaud and

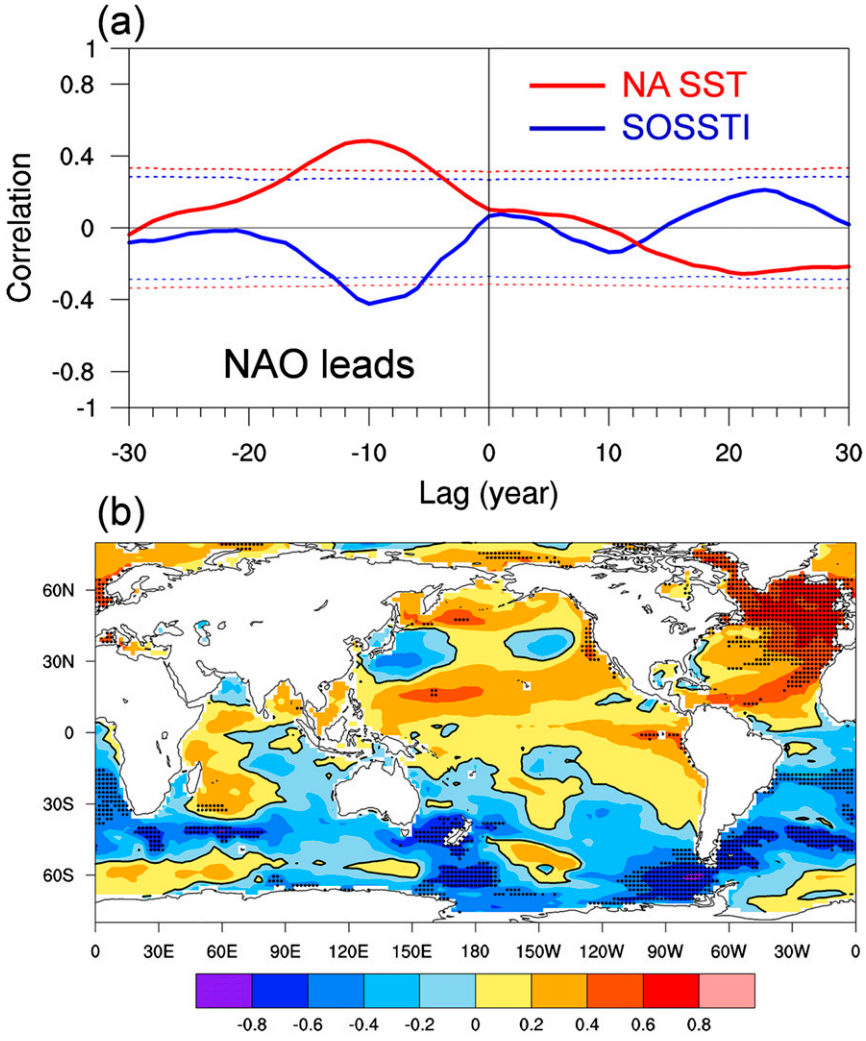

FIG. 9. (a) Cross correlations of the annual-mean NAO index with the SST average over northern North Atlantic (40°–70°N, 70°W–0°; red) and SOSSTI (65°–45°S; blue) at decadal time scales from the CCSM4 simulations. Negative (positive) lags mean that the NAO is leading (lagging). The dashed lines denote the 95% confidence level. (b) Lagged correlations of annual-mean global SST with the NAO index at decadal time scales in the CCSM4 simulations with the NAO leading by 10 yr. Dots indicate that correlations are significant at the 95% confidence level.

Wunsch 2000) and 13–19 Sv at 48°N (Ganachaud 2003). The simulated position of maximum overturning (20–25 Sv) lies at a depth of 1000–1200 m, at 40°–50°N. Thus, the CCSM4 model performs well in capturing the main features of the AMOC, and this is consistent with Wang and Zhang (2013). Figure 10b displays the lagged regression of the AMOC streamfunction onto the normalized NAO index when the NAO leads by 10 yr. The regression pattern shows significantly positive and negative anomalies north and south of 45°S, respectively, and largely resembles the long-term mean structure of the AMOC. This indicates that the AMOC tends to strengthen (weaken) about 10 yr after the NAO phase turns positive (negative). The enhanced AMOC leads to a net heat transport from the SH to the NH and stronger upwelling in the SO; as a result, it causes contrasting warm and cold SST anomalies in the North Atlantic and SO, respectively (Stouffer et al. 2006; Danabasoglu et al. 2012; Wang et al. 2014). An AMOC strength index is defined as the maximum of the annual-mean AMOC streamfunction at 40°N, similar to Zhang (2008). As expected, the AMOC is significantly positively (negatively) correlated with the area-averaged SST variations over the subpolar North Atlantic (subpolar SO) region, with a lead of the AMOC by 1–2 yr (Fig. 10c). Moreover, the lead–lag correlation between the AMOC and NAO

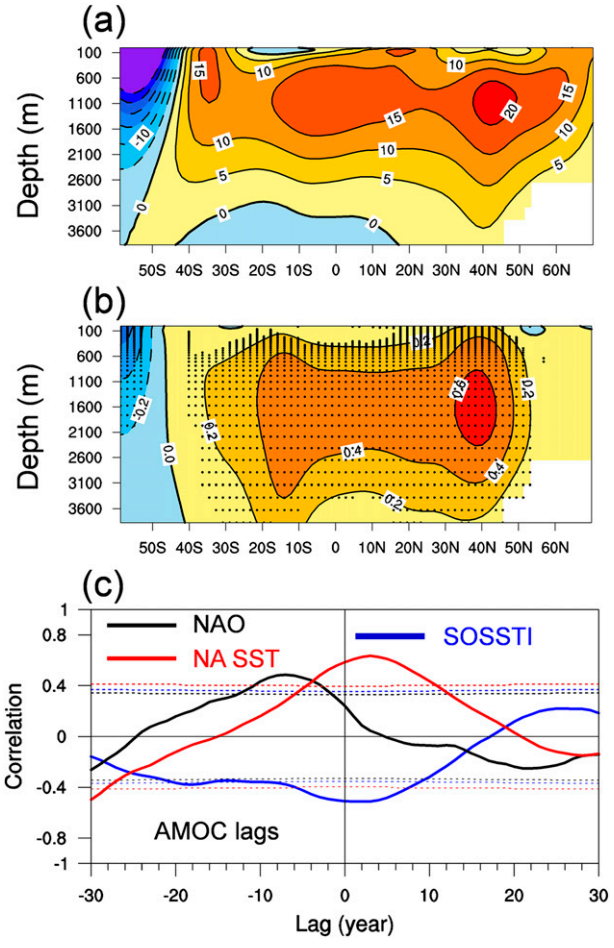

FIG. 10. (a) Long-term mean AMOC streamfunction (Sv) in the CCSM4 simulations. (b) Lagged regression of the annual-mean AMOC streamfunction (Sv) with respect to the normalized NAO index at decadal time scales, with the NAO leading by 10 yr. Dots indicate regressions significant at the 95% confidence level. (c) Cross correlations of the simulated NAO (black), SOSSTI (blue), and subpolar North Atlantic averaged SST (red) with the AMOC index at decadal time scales. Positive (negative) lags indicate that the AMOC is leading (lagging). Dotted lines denote the 95% significance level.

decadal variations (Fig. 10c) shows significantly positive values (peak correlation exceeding 0.5, significant at the 95% confidence level) at time lags of 8–9 yr (NAO leads the AMOC), further suggesting that the NAO leads the variation of AMOC strength over decadal time scales. Thus, the above analysis of the CCSM4 simulations provides further modeling evidence for the delayed influence of NAO variability on the AMOC and reveals the possible mechanisms that connect the NAO to the SO SST variations.

We also investigated how well the CCSM4 model performs at simulating the rainfall teleconnection. Figure 11a shows the lead–lag correlation between the simulated NAO and SEAR over decadal time scales. The correlation peaks at lag −10 yr (NAO leading SEAR) with the peak correlation coefficient around −0.3 (significant at the 95% confidence level). Thus, the observed decadal-scale lead of the NAO relative to the SEAR is fairly well reproduced. Figure 11b shows the simultaneous correlation map between the simulated SEAR and global SST. The correlation map shows a band of significant positive correlations in the extratropical SO (south of 45°S), in agreement with the in-phase relationship of SEAR–SO SSTs revealed in the observations. Therefore, the CCSM4 simulations support the crucial ''bridge'' role that the SO SST plays in the decadal-scale teleconnection of NAO–SEAR.

5. A simple linear model for SEAR decadal variability based on NAO and PDO

The SST–SEAR coherence in the CCSM4 simulations (Fig. 11b) also reveals a weakly negative PDO pattern in the Pacific basin. Various studies have suggested that the PDO is an important driver of eastern Australian rainfall decadal variability with the decadal coherence between ENSO and rainfall modulated by the PDO (Power et al. 1999a,b; Risbey et al. 2009; Cai et al. 2010b; Cai and van Rensch 2012) and that the negative (positive) PDO phase often coincides with wetter (drier) than average conditions across eastern Australia on a decadal time scale. Based on the observations, a negative correlation ($r = -0.48$) is observed between the PDO index and SEAR over decadal time scales for the period 1900–2013, indicating the simultaneous influence of the PDO on SEAR. In addition, the simultaneous correlation between the PDO and NAO is low and insignificant ($r = 0.30$), and no significant correlations are found when the NAO leads the PDO. This suggests that the PDO and NAO may act independently to influence SEAR decadal variability. Thus, the NAO can provide an additional physically based predictor for the SEAR besides the PDO, and the lead–lag relationship offers a simple but useful way to predict SEAR around a decade and half in advance. Moreover, this lead–lag relationship is independent of the PDO. The lead–lag correlation curves between the NAO and SEAR based on the data after removing the effect of PDO resemble those of Fig. 1b (as shown in Fig. 12a), and the correlation between the SEAR and 15-yr-ahead NAO over decadal time scales remains high ($r = -0.84$, significant at the 95% confidence level).

An empirical model for SEAR decadal variability based on the NAO and PDO was therefore developed as follows:

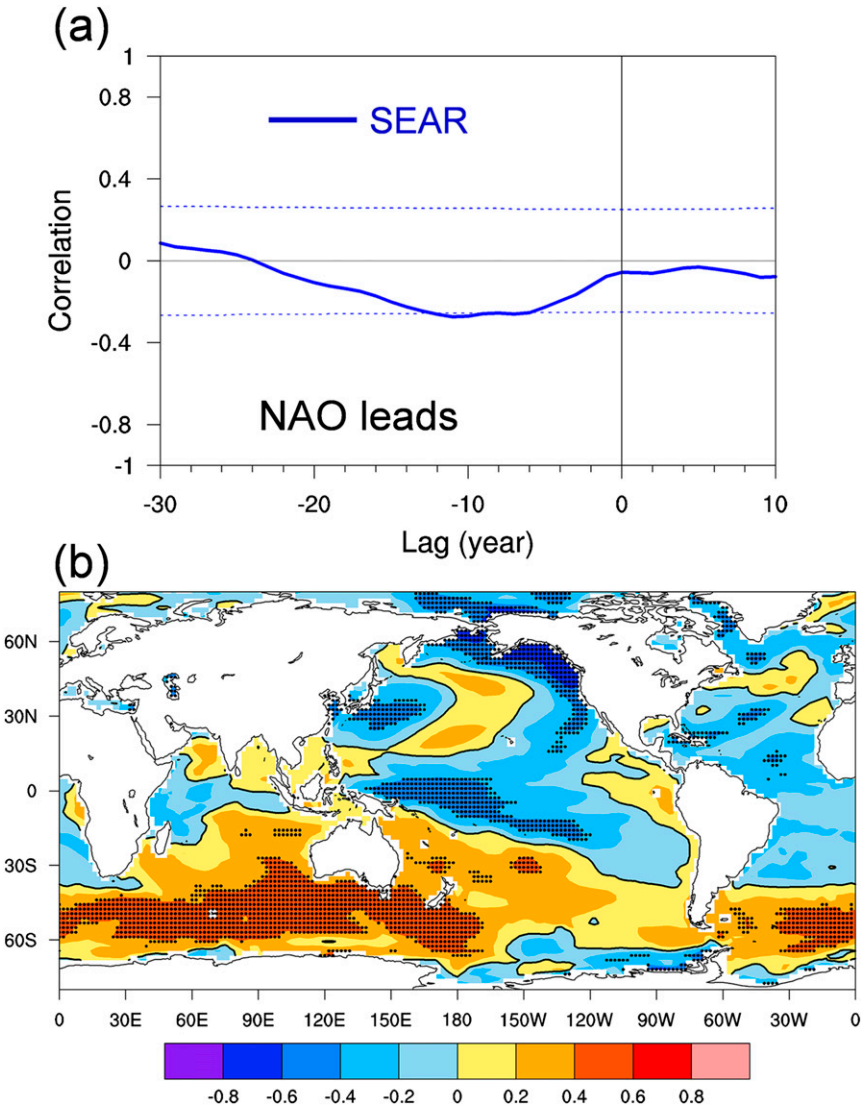

FIG. 11. (a) Cross correlations of the annual-mean NAO index with the SEAR index (area-weighted average rainfall over 45°–25°S, 135°–155°E) at decadal time scales from the CCSM4 simulations. Negative (positive) lags mean that the NAO is leading (lagging). The dashed lines denote the 95% confidence level. (b) Correlations of annual-mean global SST with the SEAR index at decadal time scales in the CCSM4 simulations. Dots indicate that correlations are significant at the 95% confidence level.

$$\mathrm{SEAR}(t) = a \times \mathrm{NAO}(t-15) + b \times \mathrm{PDO}(t) + c, \qquad (3)$$

where t is time in years and the parameters $a = -5.6$, $b = -1.6$, and $c = 0.9$ are determined empirically by linear regression based on the data over the historical period, so that the regression error of Eq. (3) is minimized. The SEAR fitted using the linear model (Fig. 12b) closely follows the observed SEAR between 1915 and 2013 ($r = 0.90$, significant at the 95% confidence level) and captures the alternating dry and wet conditions in SEA reasonably well (the sign consistency between the fitted and observed SEAR indices is around 92%). In addition, in order to access the forecast skill of the empirical model, the cross-validation method is performed by splitting the historical data in half (Newman et al. 2003). The forecasts were cross validated by removing the first (second) half from the data; computing the model parameters a, b, and c using the remaining data; and applying the parameters to make forecasts for the first (second) half. The cross-validated values of the model parameters are consistent with those based on the whole records. A high correlation ($r = 0.88$) and a small

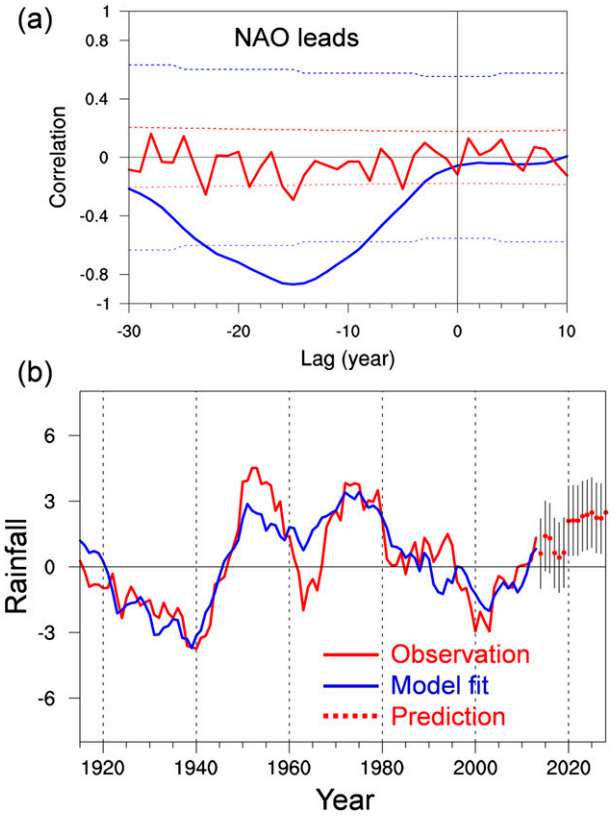

FIG. 12. (a) As in Fig. 1b, but based on the data after removing the effect of PDO (subtracting the regression onto PDO index). (b) The observed decadal SEAR from 1915 to 2013 (red), the linear model fit of SEAR (blue), and the predicted SEAR between 2014 and 2028 (red dots) assuming a fixed negative PDO phase over the next decades. Vertical bars denote the 95% confidence intervals for the predictions.

root-mean-square error ($e = 1.08\,\text{mm month}^{-1}$) are found between the observed SEAR and the cross-validated forecasts. We also performed a running correlation analysis over a 30-yr period for the observation and model simulation (1915–2013) to access the stability of the model. The running correlation is strong and stable, and the values are above 0.8 and vary by less than 0.1 (not shown here).

It should also be noted that about 20% of the variance in the smoothed SEAR is left unexplained by the model, indicating that the NAO and PDO are probably not the only factors contributing to the SEAR decadal variability. Thus, although the NAO and PDO are shown to have significant impacts on the SEAR, this does not rule out other possible factors (e.g., Indian Ocean, aerosol emissions). Several recent studies have suggested that aerosols potentially may play a role in the AMOC variability that could influence the teleconnection to the SEAR (Cai and Cowan 2007).

Since the relationship between the linear model simulation and observation is strong and stable, we carried out a prediction of SEAR for the period 2014–28. Previous studies have suggested a significant 50–70-yr periodicity in the PDO based on both instrumental and reconstruction records (Mantua and Hare 2002) and confirmed a return to the negative PDO phase since 2000 (Cai and van Rensch 2012). Thus, the negative PDO phase may possibly persist over the next two decades, and we take the value of PDO index for the prediction period 2014–28 as −0.5 (the average over the past decade). The predicted SEAR in 2014–28 and the confidence interval are shown in Fig. 12b. The combined effect of the negative PDO phase and recent NAO weakening may result in the SEAR increase over the next decades, indicating that the SEA region may experience above average rainfall in the near future.

6. Summary and discussion

Subtropical eastern Australian rainfall (SEAR) during the twentieth century shows evident decadal to multidecadal fluctuations. How best to understand and predict this SEAR decadal variability is of great significance, not only to those who study climate change but also with regard to regional water resource conditions. This paper presents observational evidence and the results of numerical simulations to demonstrate that the NAO, a pattern of atmospheric variability over the North Atlantic, can influence SEAR and leads the SEAR by around 15 yr.

Figure 13 shows a schematic of the processes that summarizes the delayed influence of NAO on the SEAR. In general, the NAO is connected to SEAR through the AMOC and Southern Ocean (SO) SSTs. The positive (negative) NAO appears to lead high-latitude SO SST cooling (warming) by about 15 yr over decadal time scales. The NAO precedes the SO SST variations because of its delayed effect on the AMOC; that is, the positive (negative) phase of the NAO tends to strengthen (weaken) the AMOC with a time lag on the order of one decade because of the large inertia associated with slow oceanic processes, and then the strengthened (weakened) AMOC in turn induces the subpolar interhemispheric SST seesaw with contrasting warm and cold (cold and warm) SST anomalies in the subpolar North Atlantic and high-latitude SO, respectively. The high-latitude SO strongly affects the SEAR over decadal time scales. Cooler (warmer) SSTs in the high-latitude SO enhance (reduce) the meridional temperature gradient and thus can excite anomalous westerlies (easterlies) in the midlatitude Southern Hemisphere (SH) and induce an anomalous cyclone

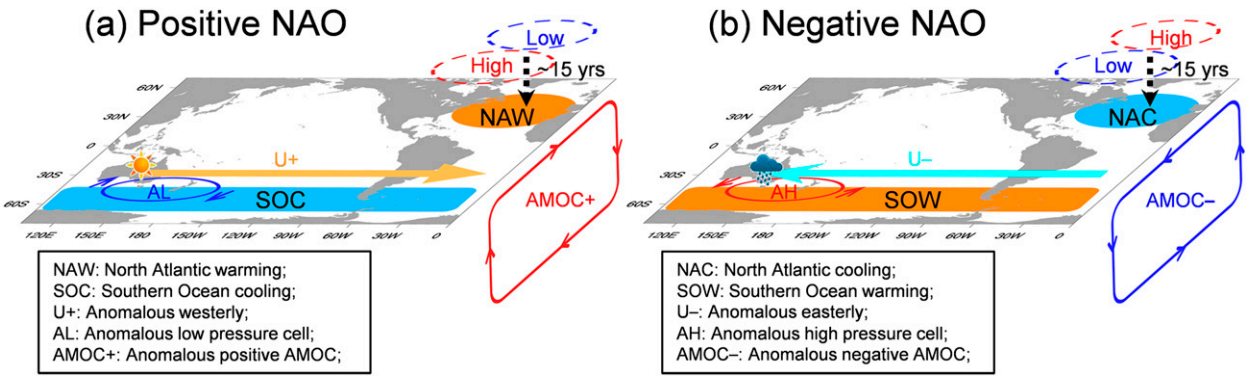

FIG. 13. Schematic diagram of the variations of the AMOC, subpolar interhemispheric SST seesaw, The SH low-level atmospheric circulation and SEAR following the (a) positive and (b) negative NAO phases, with the NAO leading by around 15 yr.

(anticyclone) south of Australia. The westerly (easterly) anomalies are unfavorable (favorable) for westward transport of water vapor from the nearby ocean to the east Australian coastal region and lead to the drier (wetter) than normal condition in subtropical eastern Australia (SEA).

The intimate linkage between the NAO and SEAR has important implications for decadal prediction of the SEAR. On the basis of the above results, an empirical linear model for SEAR decadal variability is developed by the combination of the NAO and PDO. The simulated SEAR was strongly in phase with the observation, and the relationship between model simulation and observation was stable. SEAR for the period 2014–28 may increase slightly over the coming decades, because of the recent NAO weakening and the return of the negative PDO phase.

Although the origin of decadal variations in the NAO remains under debate (Cohen and Barlow 2005), the results presented here highlight that a better understanding and improved modeling of this NAO decadal variability will be instrumental in the interpretation and future projections of SH regional climate change. The observational records are relatively short and the smoothing procedure further lowers the effective sample size and, as a result, the correlations based on smoothed data may be susceptible to possible sampling errors. However, the NAO–SEAR link is retained in the raw observational data (shown in Fig. 1b) and fairly well reproduced in a long-term simulation of air–sea coupled model, providing confidence that the NAO–SEAR teleconnection is robust to this issue. In addition, the decadal prediction scenario proposed in this study is based on annual-mean fields. However, the variability in precipitation always has a strong seasonality, and, in particular, it has been shown that the rainfall decline over southeastern Australia since the 1970s is most pronounced during the austral autumn season (Cai and Cowan 2008, 2013; Timbal and Fawcett 2013). Can this scenario predict seasonal-mean rainfall over decadal time scales? To answer this question, further exploration of the sources of predictability of seasonal-mean rainfall will be required.

Acknowledgments. The authors wish to thank the anonymous reviewers for their constructive comments. This work was jointly supported by the NSFC Projects 41305046 and 41290255 and the Youth Scholars Program of Beijing Normal University.

REFERENCES

Allan, R., and T. Ansell, 2006: A new globally complete monthly historical gridded mean sea level pressure dataset (HadSLP2): 1850–2004. *J. Climate,* **19,** 5816–5842, doi:10.1175/JCLI3937.1.

Cai, W., and T. Cowan, 2007: Impacts of increasing anthropogenic aerosols on the atmospheric circulation trends of the Southern Hemisphere: An air-sea positive feedback. *Geophys. Res. Lett.,* **34,** L23709, doi:10.1029/2007GL031706.

——, and ——, 2008: Dynamics of late autumn rainfall reduction over southeastern Australia. *Geophys. Res. Lett.,* **35,** L09708, doi:10.1029/2008GL033390.

——, and P. van Rensch, 2012: The 2011 southeast Queensland extreme summer rainfall: A confirmation of a negative Pacific decadal oscillation phase? *Geophys. Res. Lett.,* **39,** L08702, doi:10.1029/2011GL050820.

——, and T. Cowan, 2013: Southeast Australia autumn rainfall reduction: A climate-change-induced poleward shift of ocean–atmosphere circulation. *J. Climate,* **26,** 189–205, doi:10.1175/JCLI-D-12-00035.1.

——, ——, S. Godfrey, and S. Wijffels, 2010a: Simulations of processes associated with the fast warming rate of the southern midlatitude ocean. *J. Climate,* **23,** 197–206, doi:10.1175/2009JCLI3081.1.

——, P. van Rensch, T. Cowan, and A. Sullivan, 2010b: Asymmetry in ENSO teleconnection with regional rainfall, its multidecadal variability, and impact. *J. Climate,* **23,** 4944–4955, doi:10.1175/2010JCLI3501.1.

——, ——, ——, and H. H. Hendon, 2011: Teleconnection pathways of ENSO and the IOD and the mechanisms for impacts on Australian rainfall. *J. Climate,* **24,** 3910–3923, doi:10.1175/2011JCLI4129.1.

——, A. Purich, T. Cowan, P. van Rensch, and E. Weller, 2014: Did climate change–induced rainfall trends contribute to the Australian millennium drought? *J. Climate,* **27,** 3145–3168, doi:10.1175/JCLI-D-13-00322.1.

Chiang, J. C. H., and A. R. Friedman, 2012: Extratropical cooling, interhemispheric thermal gradients, and tropical climate change. *Annu. Rev. Earth Planet. Sci.,* **40,** 383–412, doi:10.1146/annurev-earth-042711-105545.

Chylek, P., C. K. Folland, G. Lesins, and M. K. Dubey, 2010: Twentieth century bipolar seesaw of the Arctic and Antarctic surface air temperatures. *Geophys. Res. Lett.,* **37,** L08703, doi:10.1029/2010GL042793.

Cohen, J., and M. Barlow, 2005: The NAO, the AO, and global warming: How closely related? *J. Climate,* **18,** 4498–4513, doi:10.1175/JCLI3530.1.

Compo, G. P., and Coauthors, 2011: The Twentieth Century Reanalysis project. *Quart. J. Roy. Meteor. Soc.,* **137,** 1–28, doi:10.1002/qj.776.

Cowan, T., P. van Rensch, A. Purich, and W. Cai, 2013: The association of tropical and extratropical climate modes to atmospheric blocking across southeastern Australia. *J. Climate,* **26,** 7555–7569, doi:10.1175/JCLI-D-12-00781.1.

Danabasoglu, G., S. G. Yeager, Y.-O. Kwon, J. J. Tribbia, A. S. Phillips, and J. W. Hurrell, 2012: Variability of the Atlantic meridional overturning circulation in CCSM4. *J. Climate,* **25,** 5153–5172, doi:10.1175/JCLI-D-11-00463.1.

Delworth, T. L., and R. J. Greatbatch, 2000: Multidecadal thermohaline circulation variability driven by atmospheric surface flux forcing. *J. Climate,* **13,** 1481–1495, doi:10.1175/1520-0442(2000)013<1481:MTCVDB>2.0.CO;2.

——, and M. E. Mann, 2000: Observed and simulated multidecadal variability in the Northern Hemisphere. *Climate Dyn.,* **16,** 661–676, doi:10.1007/s003820000075.

Dima, M., and G. Lohmann, 2010: Evidence for two distinct modes of large-scale ocean circulation changes over the last century. *J. Climate,* **23,** 5–16, doi:10.1175/2009JCLI2867.1.

Eden, C., and T. Jung, 2001: North Atlantic interdecadal variability: Oceanic response to the North Atlantic Oscillation (1865–1997). *J. Climate,* **14,** 676–691, doi:10.1175/1520-0442(2001)014<0676:NAIVOR>2.0.CO;2.

——, and R. J. Greatbatch, 2003: A damped decadal oscillation in the North Atlantic climate system. *J. Climate,* **16,** 4043–4060, doi:10.1175/1520-0442(2003)016<4043:ADDOIT>2.0.CO;2.

Enfield, D. B., and L. Cid-Serrano, 2010: Secular and multidecadal warmings in the North Atlantic and their relationships with major hurricane activity. *Int. J. Climatol.,* **30,** 174–184, doi:10.1002/joc.1881.

——, A. M. Mestas-Nunez, and P. J. Trimble, 2001: The Atlantic multidecadal oscillation and its relation to rainfall and river flows in the continental US. *Geophys. Res. Lett.,* **28,** 2077–2080, doi:10.1029/2000GL012745.

Fogt, R. L., J. Perlwitz, A. J. Monaghan, D. H. Bromwich, J. M. Jones, and G. J. Marshall, 2009: Historical SAM variability. Part II: Twentieth-century variability and trends from reconstructions, observations, and the IPCC AR4 models. *J. Climate,* **22,** 5346–5365, doi:10.1175/2009JCLI2786.1.

Ganachaud, A., 2003: Large-scale mass transports, water mass formation, and diffusivities estimated from World Ocean Circulation Experiment (WOCE) hydrographic data. *J. Geophys. Res.,* **108,** 3213, doi:10.1029/2002JC001565.

——, and C. Wunsch, 2000: Improved estimates of global ocean circulation, heat transport and mixing from hydrographic data. *Nature,* **408,** 453–457, doi:10.1038/35044048.

Gent, P. R., and Coauthors, 2011: The Community Climate System Model version 4. *J. Climate,* **24,** 4973–4991, doi:10.1175/2011JCLI4083.1.

Hansen, J., R. Ruedy, M. Sato, and K. Lo, 2010: Global surface temperature change. *Rev. Geophys.,* **48,** RG4004, doi:10.1029/2010RG000345.

Harris, I., P. D. Jones, T. J. Osborn, and D. H. Lister, 2014: Updated high-resolution grids of monthly climatic observations—The CRU TS3.10 dataset. *Int. J. Climatol.,* **34,** 623–642, doi:10.1002/joc.3711.

Hendon, H. H., D. W. J. Thompson, and M. C. Wheeler, 2007: Australian rainfall and surface temperature variations associated with the Southern Hemisphere annular mode. *J. Climate,* **20,** 2452–2467, doi:10.1175/JCLI4134.1.

Hurrell, J. W., 1995: Decadal trends in the North Atlantic Oscillation: Regional temperatures and precipitation. *Science,* **269,** 676–679, doi:10.1126/science.269.5224.676.

Jones, D. A., W. Wang, and R. Fawcett, 2009: High-quality spatial climate data-sets for Australia. *Aust. Meteor. Oceanogr. J.,* **58,** 233–248.

Knutti, R., J. Fluckiger, T. F. Stocker, and A. Timmermann, 2004: Strong hemispheric coupling of glacial climate through freshwater discharge and ocean circulation. *Nature,* **430,** 851–856, doi:10.1038/nature02786.

Kucharski, F., F. Molteni, M. P. King, R. Farneti, I. S. Kang, and L. Feudale, 2013: On the need of intermediate complexity general circulation models: A "SPEEDY" example. *Bull. Amer. Meteor. Soc.,* **94,** 25–30, doi:10.1175/BAMS-D-11-00238.1.

Latif, M., and N. S. Keenlyside, 2011: A perspective on decadal climate variability and predictability. *Deep-Sea Res. II,* **58,** 1880–1894, doi:10.1016/j.dsr2.2010.10.066.

——, R. Kleeman, and C. Eckert, 1997: Greenhouse warming, decadal variability, or El Niño? An attempt to understand the anomalous 1990s. *J. Climate,* **10,** 2221–2239, doi:10.1175/1520-0442(1997)010<2221:GWDVOE>2.0.CO;2.

——, C. Böning, J. Willebrand, A. Biastoch, J. Dengg, N. Keenlyside, U. Schweckendiek, and G. Madec, 2006a: Is the thermohaline circulation changing? *J. Climate,* **19,** 4631–4637, doi:10.1175/JCLI3876.1.

——, M. Collins, H. Pohlmann, and N. Keenlyside, 2006b: A review of predictability studies of Atlantic sector climate on decadal time scales. *J. Climate,* **19,** 5971–5987, doi:10.1175/JCLI3945.1.

——, T. Martin, and W. Park, 2013: Southern Ocean sector centennial climate variability and recent decadal trends. *J. Climate,* **26,** 7767–7782, doi:10.1175/JCLI-D-12-00281.1.

Li, J. P., 2005: Coupled air-sea oscillations and climate variations in China (in Chinese). *Climate and Environmental Evolution in China,* D. Qin Ed., China Meteorological Press, 324–333.

——, and J. X. L. Wang, 2003: A new North Atlantic Oscillation index and its variability. *Adv. Atmos. Sci.,* **20,** 661–676, doi:10.1007/BF02915394.

——, C. Sun, and F.-F. Jin, 2013: NAO implicated as a predictor of Northern Hemisphere mean temperature multidecadal variability. *Geophys. Res. Lett.,* **40,** 5497–5502, doi:10.1002/2013GL057877.

Li, Y., J. P. Li, and J. Feng, 2012: A teleconnection between the reduction of rainfall in southwest Western Australia and north China. *J. Climate,* **25,** 8444–8461, doi:10.1175/JCLI-D-11-00613.1.

Mantua, N. J., and S. R. Hare, 2002: The Pacific decadal oscillation. *J. Oceanogr.,* **58,** 35–44, doi:10.1023/A:1015820616384.

——, ——, Y. Zhang, J. M. Wallace, and R. C. Francis, 1997: A Pacific interdecadal climate oscillation with impacts on salmon production. *Bull. Amer. Meteor. Soc.,* **78,** 1069–1079, doi:10.1175/1520-0477(1997)078<1069:APICOW>2.0.CO;2.

McBride, J. L., and N. Nicholls, 1983: Seasonal relationships between Australian rainfall and the southern oscillation. *Mon. Wea. Rev.,* **111,** 1998–2004, doi:10.1175/1520-0493(1983)111<1998:SRBARA>2.0.CO;2.

Meneghini, B., I. Simmonds, and I. N. Smith, 2007: Association between Australian rainfall and the southern annular mode. *Int. J. Climatol.,* **27,** 109–121, doi:10.1002/joc.1370.

Murphy, B. F., and B. Timbal, 2008: A review of recent climate variability and climate change in southeastern Australia. *Int. J. Climatol.,* **28,** 859–879, doi:10.1002/joc.1627.

Newman, M., G. P. Compo, and M. A. Alexander, 2003: ENSO-forced variability of the Pacific decadal oscillation. *J. Climate,* **16,** 3853–3857, doi:10.1175/1520-0442(2003)016<3853:EVOTPD>2.0.CO;2.

Nnamchi, H. C., and J. P. Li, 2011: Influence of the South Atlantic Ocean dipole on West African summer precipitation. *J. Climate,* **24,** 1184–1197, doi:10.1175/2010JCLI3668.1.

——, ——, I. S. Kang, and F. Kucharski, 2013: Simulated impacts of the South Atlantic Ocean dipole on summer precipitation at the Guinea coast. *Climate Dyn.,* **41,** 677–694, doi:10.1007/s00382-012-1629-0.

Parker, D., C. Folland, A. Scaife, J. Knight, A. Colman, P. Baines, and B. W. Dong, 2007: Decadal to multidecadal variability and the climate change background. *J. Geophys. Res.,* **112,** D18115, doi:10.1029/2007JD008411.

Power, S., T. Casey, C. Folland, A. Colman, and V. Mehta, 1999a: Inter-decadal modulation of the impact of ENSO on Australia. *Climate Dyn.,* **15,** 319–324, doi:10.1007/s003820050284.

——, F. Tseitkin, V. Mehta, B. Lavery, S. Torok, and N. Holbrook, 1999b: Decadal climate variability in Australia during the twentieth century. *Int. J. Climatol.,* **19,** 169–184, doi:10.1002/(SICI)1097-0088(199902)19:2<169::AID-JOC356>3.0.CO;2-Y.

——, M. Haylock, R. Colman, and X. D. Wang, 2006: The predictability of interdecadal changes in ENSO activity and ENSO teleconnections. *J. Climate,* **19,** 4755–4771, doi:10.1175/JCLI3868.1.

Pyper, B. J., and R. M. Peterman, 1998: Comparison of methods to account for autocorrelation in correlation analyses of fish data. *Can. J. Fish. Aquat. Sci.,* **55,** 2127–2140, doi:10.1139/f98-104.

Rakich, C. S., N. J. Holbrook, and B. Timbal, 2008: A pressure gradient metric capturing planetary-scale influences on eastern Australian rainfall. *Geophys. Res. Lett.,* **35,** L08713, doi:10.1029/2007GL032970.

Risbey, J. S., M. J. Pook, P. C. McIntosh, M. C. Wheeler, and H. H. Hendon, 2009: On the remote drivers of rainfall variability in Australia. *Mon. Wea. Rev.,* **137,** 3233–3253, doi:10.1175/2009MWR2861.1.

Saji, N. H., B. N. Goswami, P. N. Vinayachandran, and T. Yamagata, 1999: A dipole mode in the tropical Indian Ocean. *Nature,* **401,** 360–363.

Schneider, U., B. Andreas, F. Peter, M.-C. Anja, R. Bruno, and Z. Markus, 2011: GPCC full data reanalysis version 6.0 at 0.58: Monthly land-surface precipitation from rain-gauges built on GTS-based and historic data. GPCC Data Rep., doi:10.5676/DWD_GPCC/FD_M_V6_050.

Smith, T. M., and R. W. Reynolds, 2005: A global merged land–air–sea surface temperature reconstruction based on historical observations (1880–1997). *J. Climate,* **18,** 2021–2036, doi:10.1175/JCLI3362.1.

——, ——, T. C. Peterson, and J. Lawrimore, 2008: Improvements to NOAA's historical merged land-ocean surface temperature analysis (1880–2006). *J. Climate,* **21,** 2283–2296, doi:10.1175/2007JCLI2100.1.

Speer, M. S., L. M. Leslie, and A. O. Fierro, 2011: Australian east coast rainfall decline related to large scale climate drivers. *Climate Dyn.,* **36,** 1419–1429, doi:10.1007/s00382-009-0726-1.

Stocker, T. F., and S. J. Johnsen, 2003: A minimum thermodynamic model for the bipolar seesaw. *Paleoceanography,* **18,** 1087, doi:10.1029/2003PA000920.

Stouffer, R. J., and Coauthors, 2006: Investigating the causes of the response of the thermohaline circulation to past and future climate changes. *J. Climate,* **19,** 1365–1387, doi:10.1175/JCLI3689.1.

Sun, C., J. P. Li, F.-F. Jin, and R. Q. Ding, 2013: Sea surface temperature inter-hemispheric dipole and its relation to tropical precipitation. *Environ. Res. Lett.,* **8,** 044006, doi:10.1088/1748-9326/8/4/044006.

Taschetto, A. S., and M. H. England, 2009: El Niño Modoki impacts on Australian rainfall. *J. Climate,* **22,** 3167–3174, doi:10.1175/2008JCLI2589.1.

Tett, S. F. B., T. J. Sherwin, A. Shravat, and O. Browne, 2014: How much has the North Atlantic Ocean overturning circulation changed in the last 50 years? *J. Climate,* **27,** 6325–6342, doi:10.1175/JCLI-D-12-00095.1.

Thompson, D. W. J., and J. M. Wallace, 2000: Annular modes in the extratropical circulation. Part I: Month-to-month variability. *J. Climate,* **13,** 1000–1016, doi:10.1175/1520-0442(2000)013<1000:AMITEC>2.0.CO;2.

Timbal, B., and R. Fawcett, 2013: A historical perspective on southeastern Australian rainfall since 1865 using the instrumental record. *J. Climate,* **26,** 1112–1129, doi:10.1175/JCLI-D-12-00082.1.

Trenberth, K. E., and D. A. Paolino Jr., 1980: The Northern Hemisphere sea-level pressure data set: Trends, errors and discontinuities. *Mon. Wea. Rev.,* **108,** 855–872, doi:10.1175/1520-0493(1980)108<0855:TNHSLP>2.0.CO;2.

Ummenhofer, C. C., M. H. England, P. C. McIntosh, G. A. Meyers, M. J. Pook, J. S. Risbey, A. S. Gupta, and A. S. Taschetto, 2009a: What causes southeast Australia's worst droughts? *Geophys. Res. Lett.,* **36,** L04706, doi:10.1029/2008GL036801.

——, A. Sen Gupta, A. S. Taschetto, and M. H. England, 2009b: Modulation of Australian precipitation by meridional gradients in east Indian Ocean sea surface temperature. *J. Climate,* **22,** 5597–5610, doi:10.1175/2009JCLI3021.1.

Visbeck, M., H. Cullen, G. Krahmann, and N. Naik, 1998: An ocean model's response to North Atlantic Oscillation-like wind forcing. *Geophys. Res. Lett.,* **25,** 4521–4524, doi:10.1029/1998GL900162.

——, E. P. Chassignet, R. G. Curry, T. L. Delworth, R. R. Dickson, and G. Krahmann, 2003: The ocean's response to North Atlantic Oscillation variability. *The North Atlantic Oscillation: Climatic Significance and Environmental Impact, Geophys. Monogr.,* Vol. 134, Amer. Geophys. Union, 113–145.

von Storch, H., and F. W. Zwiers, 1999: *Statistical Analysis in Climate Research.* Cambridge University Press, 484 pp.

Wang, C., and L. Zhang, 2013: Multidecadal ocean temperature and salinity variability in the tropical North Atlantic: Linking with the AMO, AMOC, and subtropical cell. *J. Climate,* **26,** 6137–6162, doi:10.1175/JCLI-D-12-00721.1.

——, ——, S.-K. Lee, L. Wu, and C. R. Mechoso, 2014: A global perspective on CMIP5 climate model biases. *Nat. Climate Change,* **4,** 201–205, doi:10.1038/nclimate2118.

Wanner, H., S. Brönnimann, C. Casty, D. Gyalistras, J. Luterbacher, C. Schmutz, D. B. Stephenson, and E. Xoplaki, 2001: North Atlantic Oscillation–Concepts and studies. *Surv. Geophys.,* **22,** 321–382, doi:10.1023/A:1014217317898.

Wu, Z. W., B. Wang, J. P. Li, and F.-F. Jin, 2009: An empirical seasonal prediction model of the East Asian summer monsoon using ENSO and NAO. *J. Geophys. Res.,* **114,** D18120, doi:10.1029/2009JD011733.

——, J. P. Li, Z. H. Jiang, and J. H. He, 2011: Predictable climate dynamics of abnormal East Asian winter monsoon: Once-in-a-century snowstorms in 2007/2008 winter. *Climate Dyn.,* **37** (7–8), 1661–1669, doi:10.1007/s00382-010-0938-4.

——, ——, ——, ——, and X. Zhu, 2012: Possible effects of the North Atlantic Oscillation on the strengthening relationship between the East Asian summer monsoon and ENSO. *Int. J. Climatol.,* **32,** 794–800, doi:10.1002/joc.2309.

Xie, F., J. P. Li, W. S. Tian, J. K. Zhang, and C. Sun, 2014: The relative impacts of El Niño Modoki, canonical El Niño, and QBO on tropical ozone changes since the 1980s. *Environ. Res. Lett.,* **9,** doi:10.1088/1748-9326/9/6/064020.

Yang, X., and Coauthors, 2013: A predictable AMO-like pattern in the GFDL fully coupled ensemble initialization and decadal forecasting system. *J. Climate,* **26,** 650–661, doi:10.1175/JCLI-D-12-00231.1.

Zanchettin, D., O. Bothe, W. Müller, J. Bader, and J. H. Jungclaus, 2014: Different flavors of the Atlantic multidecadal variability. *Climate Dyn.,* **42,** 381–399, doi:10.1007/s00382-013-1669-0.

Zhang, R., 2008: Coherent surface-subsurface fingerprint of the Atlantic meridional overturning circulation. *Geophys. Res. Lett.,* **35,** L20705, doi:10.1029/2008GL035463.

——, and T. L. Delworth, 2005: Simulated tropical response to a substantial weakening of the Atlantic thermohaline circulation. *J. Climate,* **18,** 1853–1860, doi:10.1175/JCLI3460.1.

——, ——, and I. M. Held, 2007: Can the Atlantic Ocean drive the observed multidecadal variability in Northern Hemisphere mean temperature? *Geophys. Res. Lett.,* **34,** L02709.

——, and Coauthors, 2013: Have aerosols caused the observed Atlantic multidecadal variability? *J. Atmos. Sci.,* **70,** 1135–1144, doi:10.1175/JAS-D-12-0331.1.